

Article

Stress Distribution Inside a Lithium-Ion Battery Cell during Fast Charging and Its Effect on Degradation of Separator

Mustapha Makki , Cheol W. Lee  *  and Georges Ayoub 

Department of Industrial and Manufacturing Systems Engineering, University of Michigan-Dearborn, Dearborn, MI 48128, USA

* Correspondence: cheol@umich.edu

Abstract: The automotive industry is rapidly transitioning to electric vehicles (EVs) in response to the global efforts to reduce greenhouse gas emissions. Lithium-ion battery (LIB) has emerged as the main tool for energy storage in electric vehicles. A widespread adoption of EVs, however, requires a fast-charging technology that can significantly reduce charging time while avoiding any unsafe conditions including short circuits due to failure of the separator in an LIB cell. Therefore, it is necessary to understand the mechanical stresses during fast charging and their long-term effect on the integrity of the separator. This paper presents a novel hybrid model for the prediction of the stress distribution in the separator of a pouch cell under various charging speeds, ambient temperatures, and pack assembly conditions, such as compressive pressures. The proposed hybrid model consists of three sub-models, namely, an electrochemical cell model, a lumped-parameter model, and a solid mechanics model. A robust parameter identification scheme is implemented to determine the model parameters using the experimental data. The separator within the test setup will experience maximum von Mises stress of 74 MPa during 4C charging, i.e., when the charge current in A is four times as high as the capacity of the battery cell in Ah. To assess the evolution of the damage in the separator under the estimated stress during fast charging, creep and fatigue tests are conducted on the separator. Their results indicate a progressive accumulation of damage in the separator, further emphasizing the importance of understanding and mitigating mechanical degradation in separator materials.



Citation: Makki, M.; Lee, C.W.; Ayoub, G. Stress Distribution Inside a Lithium-Ion Battery Cell during Fast Charging and Its Effect on Degradation of Separator. *Batteries* **2023**, *9*, 502. <https://doi.org/10.3390/batteries9100502>

Academic Editor: Quanqing Yu

Received: 16 August 2023

Revised: 26 September 2023

Accepted: 28 September 2023

Published: 2 October 2023



Copyright: © 2023 by the authors. Licensee MDPI, Basel, Switzerland. This article is an open access article distributed under the terms and conditions of the Creative Commons Attribution (CC BY) license (<https://creativecommons.org/licenses/by/4.0/>).

Keywords: hybrid model; creep and fatigue; parameter identification

1. Introduction

Due to the volatility of oil markets and strict mandates to limit greenhouse gas emissions, the automotive industry has been swiftly switching towards producing electrical vehicles as well as hybrid electric vehicles (HEVs). As the market share of EVs increases, there will be a greater demand for high efficiency energy storage systems such as lithium-ion batteries (LIBs). This is partly due to the high specific energy and energy density of LIBs, which can be two times those of other cell technologies such as nickel-metal hydride [1].

An LIB cell is composed of four main components, i.e., anode, cathode, separator, and electrolyte [2]. In an LIB cell, a critical component is the separator, which is a porous membrane positioned between the electrodes. The essential function of the separator is to prevent direct contact between the electrodes or an internal short while allowing ionic flows through the electrolyte [3]. The separator, therefore being considered the most crucial component for safety, should meet several requirements in regard to its thermal and mechanical properties. First, the separator should be chemically stable under the reductive and oxidative conditions encountered during battery operations [4]. Second, the separator should exhibit low thermal shrinkage, e.g., in an amount of less than 5% after being soaked at 90 °C for 60 min [5]. This requirement exists to avoid any exposure of electrode edges due to shrinkage of the separator at high temperatures, thereby preventing internal

shorts and thermal runaways. Moreover, the separator should melt above an elevated temperature to avoid a thermal runaway when the cell is exposed to high temperatures. A shutdown temperature of 130 °C or lower is usually required. Lastly, the separator should be mechanically robust to withstand the mechanical stresses during cell and pack assembly, operations, and any other abuse conditions [6]. Both tensile and puncture strengths of the separator should be high enough to avoid internal shorts under such conditions [7]. A gradual and up to 50% decrease in ductility of the separator was observed after the battery cell underwent 400, 800, and 1600 charge–discharge cycles involving 4C-rate charging, i.e., charging at a rate with current that is four times as high as the battery capacity [8]. A scanning electron micrograph (SEM) analysis of the cycled separators revealed accumulated damage in the separator in the form of pore closure along the thickness direction and fiber fracture and cracks along the machine direction. The degradation was attributed to the damage caused by mechanical creep which can accumulate over the cycles. Given its integral role in battery safety and functionality, an accurate characterization and modeling of the stress distribution in the separator is necessary for addressing the safety concerns under fast-charging conditions.

During battery operation, LIBs are subject to electrochemical processes, thermal energy, and mechanical stresses that may lead to safety concerns [9]. Both the electrochemical process and heat generation induce mechanical loads in the battery components. The former process induces a volumetric change of the active material due to the intercalation processes of lithium-ions, while the latter causes thermal expansion of cell components [10]. Both mechanical loads can squeeze the separator [11], which can lead to shrinkage of its pores, reduced ion transfer, and increase in internal resistance [12]. However, no practical method exists for *in situ* measurement of the stress inside the battery. Multiphysics modeling based on a finite element method is often adopted instead to predict the stress distribution. Xiao et al. [13] proposed a multiphysics and multiscale model for prediction of the stress in a polymeric separator by coupling a 1-dimensional (1-D) macroscopic battery model and a meso-scale battery sub-model. Shi et al. [14] built a multiphysics cell model for a pouch cell to predict the stress in the separator. A 1-D thermo-electrochemical cell model calculates lithium concentration and generates heat while a macroscale 2-D model of a pouch cell determines its stress distributions. However, such cell models by themselves lack the capability to predict the stress inside a cell according to its external conditions imposed by the battery pack. A battery cell will be subject to varying compressive pressure and ambient thermal conditions according to both design and use parameters of the battery pack. Swelling of a battery cell during charging and discharging and varying compressive pressure when the cell is constrained inside a battery pack are often modeled by a lumped-parameter modeling approach. Oh et al. [15] developed a thermal swelling model to predict the swelling in the battery due to temperature variation. In their other works, Oh et al. [16] used a phenomenological force and swelling model to predict the dynamic swelling in the battery. Xu et al. [17] developed a five Kelvin-Voigt elements model to characterize the viscoelastic behavior of the separator. This model enables the prediction of creep for two specific commercial separators. In their additional research, Xu et al. [18] formulated an anisotropic homogeneous model for predicting the mechanical behavior of an LIB under bending, indentation, and compression loads. Moreover, the numerical model took into account the state of charge dependence on the mechanical behavior of the lithium-ion battery (LIB). Liu et al. [19] created a multiphysics model that captures the mechanical behavior of cylindrical cells. The model also addresses short-circuit and thermal runaway behaviors. Duan et al. [20] developed a 2-D coupled multiphysics model to identify various internal short circuit modes. The model is capable of describing the entire evolution process of the battery starting from the initial deformation, triggering of internal short circuit, evolution of internal short circuit, up to the eventual thermal runaway. Yuan et al. [21] developed a generalized short-circuit criterion for two common failure modes, using volumetric strain and equivalent strain of the separator as key parameters. In this paper, a computationally efficient hybrid model is developed by linking the cell model

in [14] with a lumped-parameter model to account for the pack parameters in addition, thereby allowing optimal design of both cell and pack parameters for safety.

The proposed hybrid model consists of three main components: (1) a 1-D electrochemical model, (2) a lumped-parameter model (LPM), and (3) a 2-D solid mechanics model. The 1-D electrochemical model predicts the heat generated in the battery cell and lithium-ion concentration which are input to the LPM. The LPM represents the mechanical and thermal behaviors of a battery cell in a battery pack array. The predicted lithium-ion concentration and temperature are input to the solid mechanics model for prediction of the stress in the separator. The LPM parameters are determined via non-linear regression based on the temperature, mechanical load, and displacement data collected from a fast charging and discharging test on an LIB cell. The hybrid model, thus developed, allows calculating the stress in the separator during fast charging. New insights into damage accumulation in the separator under fast cyclic charging are obtained by performing creep and fatigue tests on the separator under the predicted stress.

This paper is organized as follows: Section 2 describes the hybrid model proposed in this study. Then, Section 3 provides detailed explanation on the material properties of the tested LIB cell and the testing setup. Section 4 presents the experimental results along with the parameter identification process. In Section 5, a simulation study is conducted using the developed model to check the effect of charging rate, pack assembly condition, and ambient temperature on the stress induced in the separator. Section 6 focuses on presenting the results of creep and fatigue tests conducted under the predicted stress during fast charging. Finally, the conclusion is presented in Section 7.

2. Hybrid Model

During a charge and discharge cycle, an LIB cell is subject to electrochemical, thermal, and mechanical phenomena occurring simultaneously. Each phenomenon is described by a set of equations and coupled with others. The framework of the proposed hybrid model is divided into three components. The first component is a 1-D model for predicting transport of lithium-ions, electrochemical reactions, and generated heat given charge and discharge rates. The 1-D model is composed of three domains of anode, separator, and cathode. The second model component is a lumped-parameter model (LPM) that will predict the load, displacement, and temperature in the battery cell and its fixture. This model is composed of three parts: a thermal model for heat transfer, a spring model for the mechanical forces, and a linking equation which links the thermal model to the spring model. The LPM takes both predicted heat and state of charge (SOC) from the 1-D electrochemical model as inputs. Additional input variables of the LPM include ambient temperature and pre-torque on the fixture. The third component is a 2-D solid mechanics model which will calculate the stress distribution in the separator given (1) cell core temperature and boundary pressure predictions from the LPM and (2) lithium concentration in the electrodes as predicted by the 1-D battery model. Figure 1 shows all three components with the input/output variables. In what follows, a detailed description of each model component is provided.

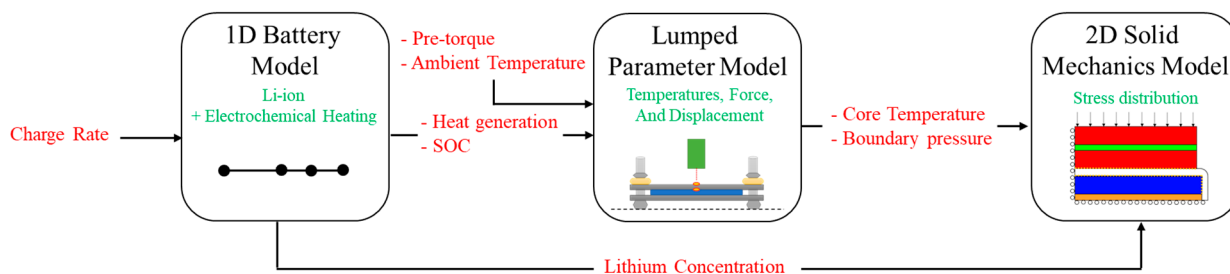


Figure 1. Flowchart of the hybrid model.

2.1. One-Dimensional (1-D) Battery Model

The 1-D battery model, shown in Figure 2, accounts for the electrochemical reaction and heat generation in a battery cell. An LIB cell Li-ion is composed of three components placed in the electrolyte, namely, cathode, anode, and separator.

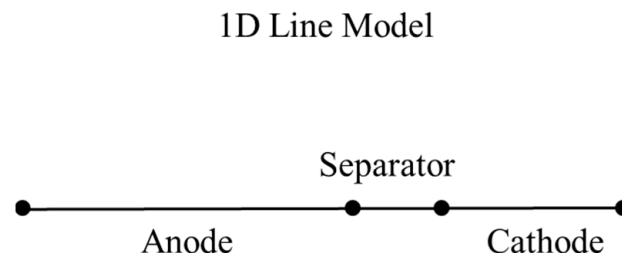


Figure 2. One-dimensional (1-D) electrochemical model.

The volume fraction of the electrodes is defined by:

$$\varepsilon_l^i = 1 - \varepsilon_s^i - \varepsilon_{filler}^i \quad (1)$$

where ε_s^i is the active material volume fraction, ε_l^i is the electrolyte volume fraction (porosity), and ε_{filler}^i denotes the binder and filler volume fraction. The superscript i denotes the electrode under consideration (p for positive electrode and n for negative electrode). In what follows, the governing equations for the diffusion, kinetics, and charge conservation [22,23] are summarized for the solid and electrolyte phases.

2.1.1. Solid Phase

The following equations apply to the solid phase of the anode and cathode. The active material in the electrodes is assumed to be composed of spherical particles. The Fick's second law describes the transport in the solid electrode particles and predicts the change of concentration field with time in spherical coordinates:

$$\frac{\partial c_s^i}{\partial t} = \frac{D_s^i}{r^2} \frac{\partial}{\partial r} \left(r^2 \frac{\partial c_s^i}{\partial r} \right) \quad (2)$$

where r is the particle radius coordinate, c_s^i is the lithium concentration in the solid particle phase, and D_s^i is the diffusion coefficient of lithium-ion in solid electrode particles. The equation assumes a constant diffusion coefficient of lithium-ions in the solid phase. According to the symmetry condition, the first boundary condition yields $-D_s^i \frac{\partial c_s^i}{\partial r} \Big|_{r=0} = 0$ since there is no flux at the center of the particle. The second boundary condition relates the pore wall flux across the interface and the rate of diffusion of lithium-ions into the solid/liquid interface, yielding $-D_s^i \frac{\partial c_s^i}{\partial r} \Big|_{r=r_p} = J^i$, where r_p is the particle radius and J^i is the pore wall flux of lithium-ions defined through the Butler–Volmer equation (Equation (6)).

The conservation of charge in the solid phase is governed by Ohm's law:

$$\frac{\partial}{\partial x} \left(\tau_{eff}^i \frac{\partial \phi_s^i}{\partial x} \right) = a_v F_r J^i \quad (3)$$

where τ_{eff}^i is the effective conductivity determined by $\tau_{eff}^i = \varepsilon_s^{i,1.5} \tau_s^i$, ϕ_s^i is the potential in the solid phase, a_v is the particle specific surface area, and F_r denotes the Faraday's constant. The first boundary condition applies to the interface between the current collector and the positive electrode, where the charge flux is equal to the current density I_{app} , i.e., $-\tau_{eff}^i \frac{\partial \phi_s^i}{\partial x} \Big|_{x=0} = I_{app}$. The second boundary condition exists at the interface between the electrodes and separators which corresponds to no charge flux:

$-\tau_{eff}^i \frac{\partial \phi_s^i}{\partial x} \Big|_{x=L_N} = -\tau_{eff}^i \frac{\partial \phi_s^i}{\partial x} \Big|_{x=L_N+L_{sep}} = 0$, where L_N and L_{sep} are the negative electrode and separator thicknesses, respectively.

2.1.2. Liquid Phase

The following equations apply to the electrolyte in the electrodes and separator. To account for lithium species transport in the liquid, the concentrated solution theory is adopted [22,24,25]. The material balance for a salt in liquid phase is given by:

$$\varepsilon_l^v \frac{\partial c_l^v}{\partial t} = \frac{\partial}{\partial x} \left(D_{eff,l}^i \frac{\partial c_l^v}{\partial x} \right) + (1 - t_+) a_v j^i \quad (4)$$

where ε_l^v denotes the electrolyte volume fraction in the component v , c_l^v is the lithium concentration in the electrolyte, $D_{eff,l}^i$ is the effective diffusion coefficient in the electrolyte given by $D_{eff,l}^i = \varepsilon_l^{i,1.5} D_l^i$, and t_+ is the transport number. The superscript v denotes the component under consideration (p for cathode, n for anode, and sep for separator). For the separator, the pore wall flux is set to zero. No mass flux occurs at the two ends of the cell, hence $\frac{\partial c_l^v}{\partial x} \Big|_{x=0} = 0$ and $\frac{\partial c_l^v}{\partial x} \Big|_{x=L} = 0$.

The charge balance in the liquid phase is based on Ohm's law:

$$-\frac{\partial}{\partial x} \left(\kappa_{eff,i} \frac{\partial \phi_l^i}{\partial x} \right) + \frac{2RT(1-t_+)}{F} \frac{\partial}{\partial x} \left(\kappa_{eff,i} \frac{\partial (\ln c_l^v)}{\partial x} \right) = a_v F_r J^i \quad (5)$$

where $\kappa_{eff,i}$ is the effective conductivity, ϕ_l^i is the potential in the liquid phase, R is the ideal gas constant, and T is the temperature. At the two ends of the cell, there is no current flow in the liquid phase, i.e., $\frac{\partial \phi_l^i}{\partial x} \Big|_{x=0} = \frac{\partial \phi_l^i}{\partial x} \Big|_{x=L} = 0$.

2.1.3. Charge Transfer

The pore wall flux at the interface between the electrode and electrolyte is determined by the Butler–Volmer equation which describes the relationship between the electrical current, electrode potential, and local concentration at the interface. Specifically, the rate of transfer of lithium-ions from the electrolyte to an electrode is controlled by deviation of the surface potential from its equilibrium value as follows:

$$j^i = a_v i_{ex} \left(\exp \left(\frac{\alpha_a F_r \eta^i}{RT} \right) - \exp \left(\frac{-\alpha_c F_r \eta^i}{RT} \right) \right) \quad (6)$$

where i_{ex} is the exchange current density, η^i is the overpotential of the intercalation reaction, and α_a and α_c are the charge transfer coefficients for oxidation and reduction, respectively, which are assumed to be 0.5. Both the forward rate of the anodic process and the backward rate of the cathodic process are given in Equation (6). The exchange current density is given by:

$$i_{ex} = F_r k_i \left(\frac{c_l^i}{c_{l,ref}} \right)^{\alpha_a} \left(c_{s,max}^i - c_{s,surf}^i \right)^{\alpha_c} \left(c_{s,surf}^i \right)^{\alpha_a} \quad (7)$$

where k_i is the reaction rate constant, c_l^i is the concentration of lithium-ions in the electrolyte, $c_{s,surf}^i$ is the concentration of lithium-ions on the surface of the solid electrode, and $c_{s,max}^i - c_{s,surf}^i$ is the available space for lithium intercalation.

The overpotential is given by:

$$\eta^i = \phi_s^i - \phi_l^i - U^i \quad (8)$$

where ϕ_s^i is the potential of the solid electrode, ϕ_l^i is the potential of the electrolyte, and U^i is the open circuit potential.

2.1.4. Heat Generation

Two main mechanisms of heat generation are considered in this study, namely, reversible entropy heat and irreversible joule heat. The corresponding equation for heat generation rate, Q_{gen} , is as follows:

$$Q_{gen} = \left(\phi_s^i - \phi_l^i - U^i + T \frac{\partial U^i}{\partial T} \right) J \quad (9)$$

where $(\phi_s - \phi_l - U_i)J$ represents the joule heat while $T \frac{\partial U_i}{\partial T} J$ represents the entropy heat.

2.2. Lumped-Parameter Model

In a lumped-parameter model, a battery cell is represented based on equivalent material properties such as thermal conductivity and specific heat [15,26,27]. In addition, a uniform heat generation is assumed throughout the battery cell [28–30].

2.2.1. Thermal Model

A schematic diagram of the pouch cell sandwiched between two fixture plates is shown in Figure 3. The lumped-parameter model assumes a 1-D thermal behavior of the pouch cell with a conduction boundary condition via contacts with the plates. Moreover, a convective boundary condition exists on both the top and bottom of the plates.

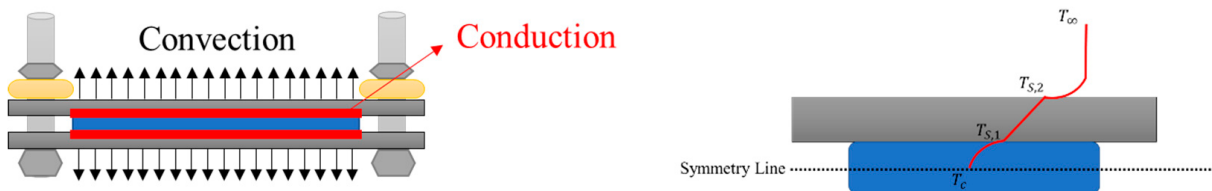


Figure 3. Schematic representation of the pouch cell inside the fixture.

The transient one-dimensional conductive heat transfer equation is as follows:

$$C_{cell} \frac{dT_C(t)}{dt} = Q_{gen}(t) - 2 \times \frac{K_{cell} A_{cell}}{\frac{L_{cell}}{2}} (T_C(t) - T_{S,1}(t)) \quad (10)$$

where C_{cell} is the cell heat capacity, $Q_{gen}(t)$ is the heat generated in the battery, T_C is the core temperature of the battery, and $T_{S,1}(t)$ is the surface temperature of the battery while K , A , and L denote the thermal conductivity, area, and length, respectively. The convective heat transfer at the top boundary of the plate can be expressed as:

$$Q_{conv} = h_{air} A_{plate} (T_{S,2}(t) - T_\infty) \quad (11)$$

Moreover, a two-state representation of the 1-D thermal model is given by:

$$\frac{K_{cell} A_{cell}}{\frac{L_{cell}}{2}} (T_C(t) - T_{S,1}(t)) = \frac{K_{plate} A_{plate}}{\frac{L_{plate}}{2}} \left(T_{S,1}(t) - \frac{T_{S,1}(t) + T_{S,2}(t)}{2} \right) \quad (12)$$

$$\frac{K_{cell} A_{cell}}{\frac{L_{cell}}{2}} (T_C(t) - T_{S,1}(t)) = h_{air} A_{plate} (T_{S,2}(t) - T_\infty) \quad (13)$$

where $T_{S,2}(t)$ is the surface temperature of the plate, T_∞ is the ambient temperature, and h_{air} is the air convection coefficient.

2.2.2. Spring Model

A spring model was developed to represent the mechanical behavior of a battery cell in the fixture. Figure 4 illustrates the behavior of the cell at constrained conditions. Two equivalent stiffness elements are adopted, i.e., the equivalent stiffness s_{Total} , representing the cell and the plate, and the equivalent stiffness s_{Rod} , representing the rod. These equivalent stiffness values refer to the relationship between the force applied on the fixture and the displacement of the fixture along the vertical axis. A linear model is adopted to predict the dependence of the force on the displacement (Branch A):

$$F_{Branch\ A} = s_{Total} (\delta_{Total}^{c,\%}) \quad (14)$$

where s_{Total} is the linear equivalent stiffnesses, and $\delta_{Total}^{c,\%}$ represents the constrained displacement of the battery and plates. The superscript c represents the constrained displacement conditions. There are four rods connected in parallel at the four edges of the plate. The total force in Branch B can be described by:

$$F_{Branch\ B} = 4 \times s_{Rod} (\Delta_{bolt} + \delta_b^{f,\%} - \delta_{Total}^{c,\%}) \quad (15)$$

where Δ_{bolt} is the displacement in the rod due to the tightening of the bolt and $\delta_b^{f,\%}$ is the free unconstrained displacement of the battery. The total measured displacement is given by:

$$\delta^{EXP,\%} = \delta_b^{f,\%} - \delta_{Total}^{c,\%} + \delta_0^c \quad (16)$$

where δ_0^c is the initial displacement.

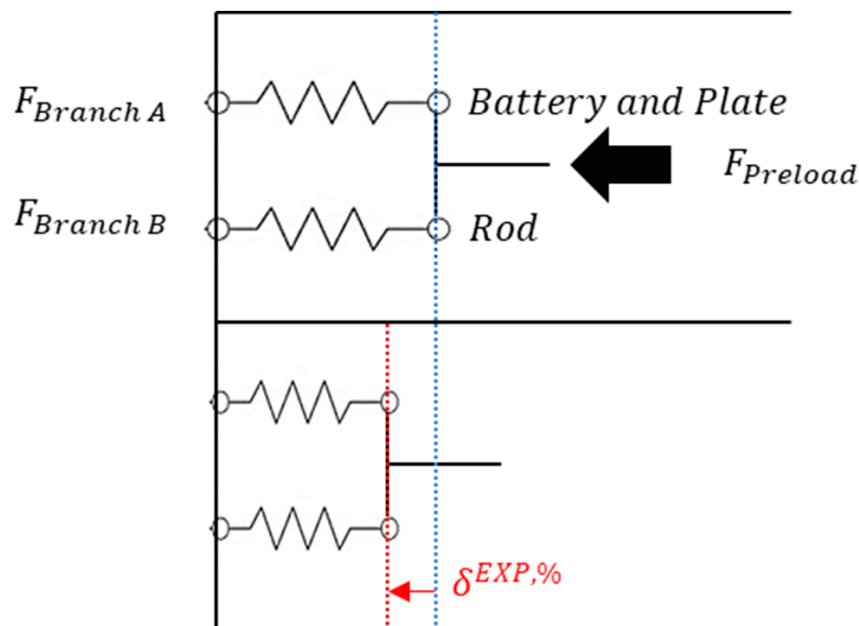


Figure 4. Spring model.

At equilibrium, the plate and the battery cell will be compressed while the four rods will be stretched. Therefore, the plates and the battery cell will be under compressive force and the rods will be subject to tensile force. At mechanical equilibrium, these two forces will be equal:

$$F_{Branch\ A} = F_{Branch\ B} \quad (17)$$

2.2.3. Coupling between Thermal and Mechanical Models

In the proposed LPM, the total swelling of the battery cell, ΔL_{Total} , consists of (1) swelling due to thermal expansion, $\Delta L_{Thermal}$, and (2) swelling due to Li-ion intercalation process, $\Delta L_{Intercalation}$. Assuming uniform heat generation across the cell, the temperature distribution in the battery will follow a parabolic shape (See Figure 3). The thermal swelling normal to the battery cell is given by:

$$\Delta L_{Thermal} = \alpha \int_0^{L_{Cell}} (T(x) - T_S) dx \quad (18)$$

where ΔL_T is the thermal swelling (due to the cell heating/cooling), L_{Cell} is the thickness of the cell, α is the lumped coefficient of thermal expansion, and T is the temperature. The subscript S denotes the surface initial state. Integrating Equation (18) based on the parabolic temperature distribution across the cell gives:

$$\Delta L_{Thermal}(t) = \alpha \times L_{Cell} \times \left(\frac{2}{3} (T_C(t) - T_S(t)) + (T_S(t) - T_{Ref}) \right) \quad (19)$$

where $T_C(t)$, $T_S(t)$, and T_{Ref} denote cell-core temperature, cell-surface temperature, and reference temperature, respectively. Swelling due to the Li-ion intercalation during charging and discharging is represented by a linear equation:

$$\Delta L_{Intercalation} = \xi \cdot SOC \quad (20)$$

where ξ is the coefficient of expansion according to the state-of-charge (SOC) of the cell. An average SOC over thickness was used in this model.

The thermal model in Section 2.2.1 and the spring model in Section 2.2.2 are linked via the free swelling term as follows:

$$\begin{aligned} \delta_b^{f,\%} &= \Delta L_{Thermal} + \Delta L_{Intercalation} = \\ &\alpha_{Battery} L_{Battery} \left(\frac{2}{3} (T_c - T_{s,1}) + (T_{s,1} - T_{Ref}) \right) + \xi \cdot SOC \end{aligned} \quad (21)$$

2.3. Solid Mechanics Model

A 2-D solid mechanics model is adopted to predict the stress in a battery cell. The model was developed in COMSOL Multiphysics 5.6. Schematic representation of the mechanics model for a pouch cell is shown in Figure 5. The part modeled is highlighted using a dotted box. The negative current collector, anode electrode, separator, cathode electrode, and positive current collector are shown in different colors. Two types of boundary conditions exist in the model, namely, internal and external boundary conditions. During battery production, the separator is tightly wrapped around the electrodes after electrodes and current collectors are bonded together. Therefore, a set of bonded electrode and current collector is considered as a continuous medium. In contrast, a contact-type boundary condition, allowing a slip at the interface, was assigned between cathode and separator and between anode and separator, respectively. External boundary conditions include a symmetric boundary condition on the left and bottom side of the model and a free boundary on the right side. Three main inputs were used in the solid mechanics model; a distributed normal load is applied at the top according to the predicted force on the battery and fixture plates by the LPM, i.e., $F_{Branch A}$ (see Figure 4). Additionally, the core temperature from the LPM is assumed to be uniform throughout the solid mechanics model since the cell is very thin [14], and an average lithium concentration was used for the electrodes.

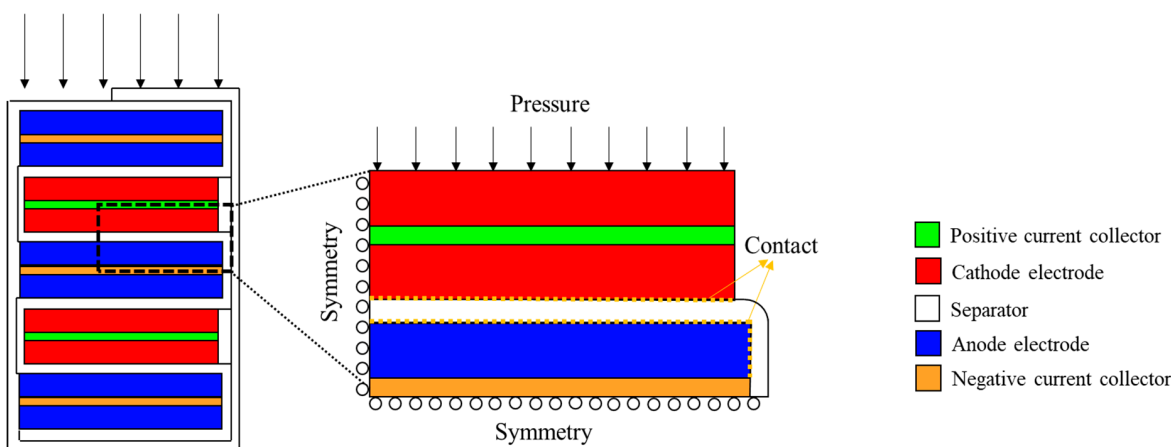


Figure 5. Schematic representation of a 2-D mechanics model.

Remark 1. The 2D mechanics model includes an extra cathode on the top for counter bending of the existing cathode. Without an extra cathode on top of the positive current collector, the cathode below will form an asymmetric beam which tends to deflect upward away from the separator due to intercalation-induced stresses.

The constitutive equations of the model include those based on mechanical strains ε_{ij}^{me} , thermal strain ε_{ij}^T [14], and intercalation-induced strain ε_{ij}^D [13,31] to predict the stress in the battery components as follows:

$$\begin{aligned}\varepsilon_{ij} &= \varepsilon_{ij}^{me} + \varepsilon_{ij}^T + \varepsilon_{ij}^D \\ &= \frac{1}{E^v} ((1 + \nu^v) \sigma_{ij} + \nu \sigma_{kk} \delta_{ij}) + \alpha_{ij} \Delta T \delta_{ij} + \frac{1}{3} \Delta c \Omega \delta_{ij}\end{aligned}\quad (22)$$

where E^v is the Young's modulus, ν^v is the Poisson's ratio, σ_{ij} is the stress tensor, and δ_{ij} is the Kronecker delta, α_{ij}^v is the thermal expansion coefficient, ΔT is the change in temperature from a reference value, Δc is the change in the diffusion species concentration from a reference (stress-free) value, and Ω^i is the partial molar volume [31,32]. The partial molar volume can be calculated using [31]:

$$\Omega^i = \frac{3\varepsilon}{\Delta y C_{s,Max}} \quad (23)$$

Remark 2. Equation (22) only considers elastic deformation and does not consider any plastic deformation. This is a safe assumption since the amount of deformation in this study is very small and does not exceed the elastic limit [8,14,33–35]. It should be also noted that the strain induced by intercalation, denoted by ε_{ij}^D is exclusively applicable to the positive and negative electrodes. Additionally, Equation (22) considers a constant Young's modulus in the mechanical strains for the electrodes. The Young's modulus was considered independent of the lithium concentration. In [36], the authors showed that elastic stiffening increases the elastic modulus, which increases the stress. However, to maintain simplicity in this work, no concentration-dependent material properties were considered.

3. Experimental Setup

3.1. Battery Cell

A pouch LIB cell with a size of 110 mm by 74 mm is tested in this study. The battery cell with a capacity of 3.5 Ah is built on mesophase graphite (SMG) anode and LiNi_{0.6}Co_{0.2}Mn_{0.2}O₂ (NMC 622) cathode, 1 M LiPF₆ in ethylene carbonate (EC): ethyl

methyl carbonate (EMC) (3:7 by volume) for electrolyte, and wet-processed polyethylene (PE) single-layer separator.

More details about the PE separator are as follows. The PE separator (12 μm thick) is fabricated through a co-extrusion blowing process. The separator porosity is 43% with a crystallinity ranging between 60% and 80%. The tensile strength in the machine direction (MD) is 235 MPa while that in the transversal direction (TD) is 225 MPa. The PE separator properties are summarized in Table 1.

Table 1. PE separator properties.

Thickness (μm)	Crystallinity (%)	Porosity (%)	Heat Shrinkage MD (% @105C, 8 h)	Heat Shrinkage TD (% @105C, 8 h)	Tensile Strength MD (MPa)	Tensile Strength TD (MPa)
12	60–80	43	4.0	4.5	235	225

In a battery cell, the pores in the electrodes and separator are filled with electrolyte. Therefore, the effective thermal expansion coefficient and Young's modulus of the electrodes and separator were calculated considering their porosities. The effective thermal expansions of the electrodes and separator were estimated by the rule of mixture as follows:

$$\alpha_{eff} = \sum_i \alpha_i V_i \quad (24)$$

where α_i and V_i are the thermal expansion coefficient and the volume fraction of the i th phase, respectively. The effective Young's modulus can be calculated in a similar manner.

The material properties for the 1-D battery cell model and the 2-D solid mechanics model are listed in Table 2. The use of '*' next to a value indicates that it is an effective material property.

Table 2. Material properties for 1-D battery cell and 2-D solid mechanics models.

Model Parameters	Units	Cu	Anode	Separator	Cathode	Al	Electrolyte
Dimensional Parameters							
Thickness	μm	10	71	12	48.5	20	
Length	mm	71	71		69	69	
Electrochemical Parameters							
Density	kg/m^3		2230	900	4750		1210
Active volume fraction			0.5686		0.6698		
Porosity			0.37454	0.43	0.26322		
Stoichiometric maximum concentration	mol/m^3		49,000		31,507		
Diffusion coefficient	m^2s^{-1}		1.4523×10^{-13}		5×10^{-13}		
Particle radius	μm		4		5		
Partial molar volume	m^3/mol		4.4196×10^{-5}		2.8418×10^{-5}		
Thermal Parameters							
Thermal expansion coefficient	$1/\text{K}$	17×10^{-6}	$6.03 \times 10^{-6} *$	$82.5 \times 10^{-6} *$	$9.62 \times 10^{-6} *$	23×10^{-6}	
Mechanical Parameters							
Young's modulus	GPa	110	6.82 *	0.645 *	6.69 *	70	
Poisson's ratio		0.35	0.3	0.45	0.3	0.33	0.25

3.2. Cell Fixture and Instrumentation

A fixture, shown in Figure 6, was used to emulate a battery module assembly. The fixture was built by holding two steel plates (each with a size of 125 mm × 99 mm × 12.7 mm) with four threaded rods (9.5 mm in diameter). A thermocouple was attached on the top of the battery cell to measure the cell surface temperature while another thermocouple was installed on the top of the upper plate. An additional thermocouple was used to monitor the ambient temperature. Four compression load cells (Omega LC9150-500-1K) were placed between the upper plate and hex nuts. A high precision displacement sensor (Keyence LK-G10) was placed 10 mm above the upper plate to measure the expansion of the battery cell. The whole setup was placed inside a thermal chamber whose temperature was set to 20 °C. After the battery cell was charged at a constant current—constant voltage (CC–CV) to 3.6 volts at 0.5 C, with a 5% current cutoff (0.0875 A), it was allowed to rest for 1 h for thermal equilibrium. Then, a pre-torque in the amount of 1 Nm was applied on each hex nut to compress the battery cell.

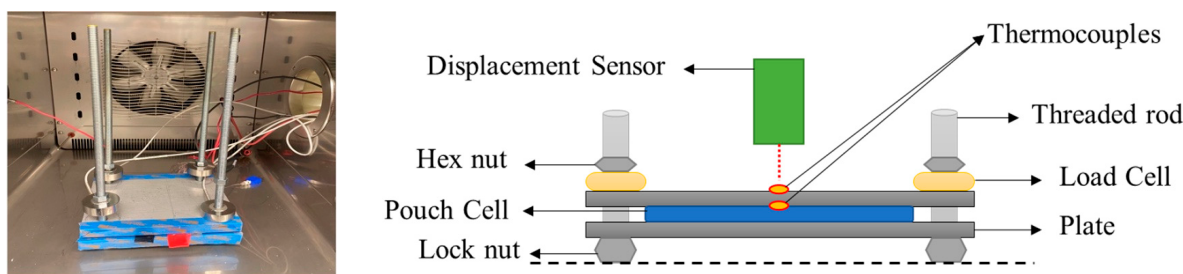


Figure 6. Experimental setup.

4. Identification of LPM Parameters

This section describes how the parameters of the lumped-parameter model (LPM) are identified.

4.1. Experiments for Measurement of Stiffness

Both force and displacement were measured under several torques to find the equivalent spring constant of battery cell and plates. The fixture shown in Figure 6 was used for the experiment. The battery was initially charged to 3.6 volts and placed between the plates. No thermocouples were used in this experiment. Four compression load cells (Omega LC9150-500-1K) were placed between the upper plate and hex nuts. The torque on each hex nut was increased by an increment of 0.2 N·m from 0 to 1 N·m and by an increment of 0.1 N·m from 1 to 1.2 N·m. Force and displacement measurements were recorded at each increment. The equivalent stiffness was fitted on the force and the displacement experimental data are shown in Figure 7a. The spring constant for the battery was found to be $s_{Total} = 9.0892 \times 10^6 \text{ N}\cdot\text{m}^{-1}$.

Another experiment was carried out to find the stiffness coefficient of the threaded rod. A rod was placed vertically with a lock-nut at the bottom. An Omega load cell was placed between the lock-nut and a hex nut. As the applied torque on the hex nut increased from 0 to 1.6 N·m, the force and elongation of the rod were measured. The rod spring constant was fitted on the force and the elongation data are shown in Figure 7b. The turn angle was used to calculate the elongation in the rod using the pitch. Note this spring constant corresponds to the portion of the rode between the two nuts. The Young's modulus can then be found using:

$$S_{Rod} = \frac{EA}{L} \quad (25)$$

Using the Young's Modulus, we can then calculate the spring constant of the rod for its length in the fixture. The spring constant for the rod was found to be $S_{Rod} = 1.0311 \times 10^7 \text{ N}\cdot\text{m}^{-1}$.

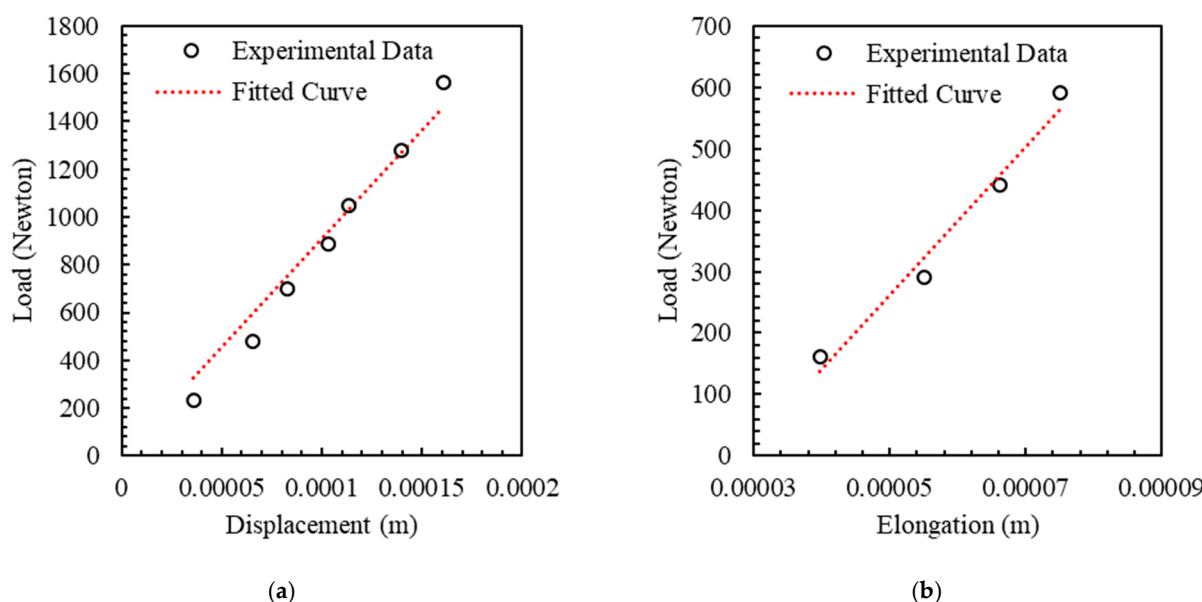


Figure 7. (a) Force versus displacement for the equivalent battery and plate spring constant and (b) rod spring constant.

4.2. Charging and Discharging Test

The force, displacement, and temperatures during charging and discharging were measured after the battery cell was installed in the fixture described in Section 3.2. The collected data were used for tuning the LPM parameters as described in Section 4.3. The test was performed under ambient temperature of 20 °C.

The battery was initially charged to 3.6 volts with a constant current of 1.75 A (0.5C), and then the voltage was held at 3.6 volts until the current dropped to 5% of its initial value. Figure 8a shows the voltage and current at the start of discharge from 3.6 volts. The data consist of three parts based on constant current–constant voltage (CC–CV) protocols. The first part of the curve shows CC–CV discharging at 0.5C from 3.6 to 3 volts (0–2178 s). The second part is a period of CC–CV fast charging at 4C from 3 to 4.2 volts (2179–3407 s), and the third part corresponds to CC–CV discharging at 0.5C from 4.2 to 3 volts (3408–9470 s). Figure 8 also shows variations of load and displacement overlayed on the voltage curve. Starting with the displacement figure (see Figure 8b), the discharge between 3.6 volts and 3 volts decreases the displacement (height) of the top surface of the fixture due to shrinkage of the battery cell. During the period of fast charging at 4C, a sharp increase in the displacement due to rapid expansion of the battery cell can be observed. During the voltage-hold period after fast charging, a small increase in the displacement is followed by a decrease. This is due to an initial increase in the temperature during charging followed by a decrease, causing cell shrinkage, during the hold period. The maximum displacement reached during fast charging was 45.8 μm. During discharging, the displacement decreases sharply between 4.2 volts and 3.7 volts, followed by a small decrease between 3.7 and 3.6 volts and another sharp decrease between 3.6 and 3 volts. The load follows the same trend of the displacement curve. After tightening the bolts with a 1 N·m torque, the initial load applied on the battery was 1314 N at the beginning of the test. The load decreases to 983 N during the first discharging, then increases significantly during charging to reach 2333 N at maximum followed by a small decrease to 2213 N during the hold period. During the second discharging period, the load decreases to 1070 N.

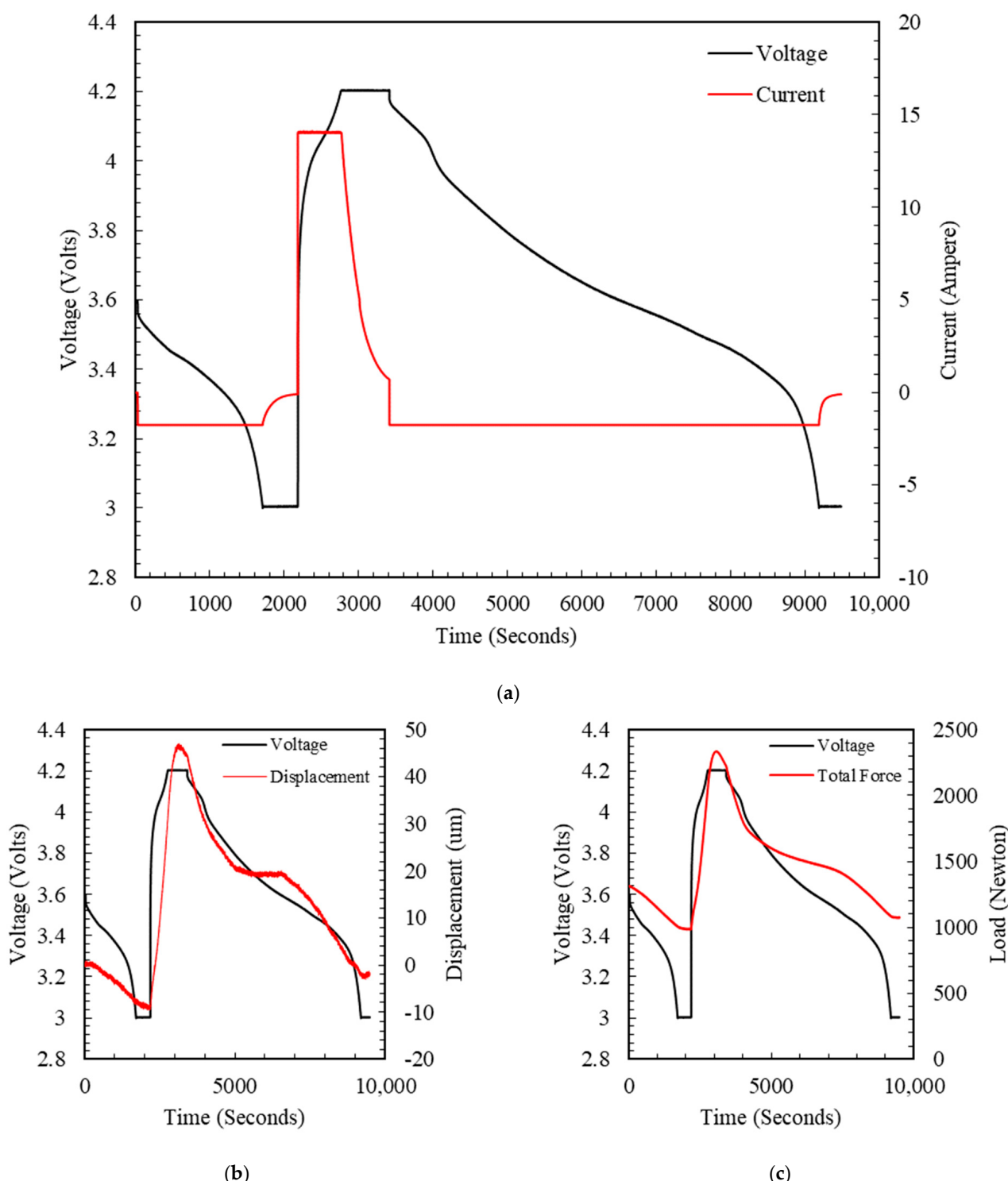


Figure 8. Variations of voltage, current, displacement, and force over time. (a) Voltage and current. (b) Voltage and displacement. (c) Voltage and load.

Figure 9 presents the battery-surface and plate-surface temperatures measured during the fast-charging period. During fast charging at 4C, an increase can be seen in both temperatures. At an ambient temperature of 20 °C, the battery-surface and plate-surface temperatures reached 21 and 20.8 °C, respectively. During the following hold period, both temperatures decreased approaching the ambient temperature.

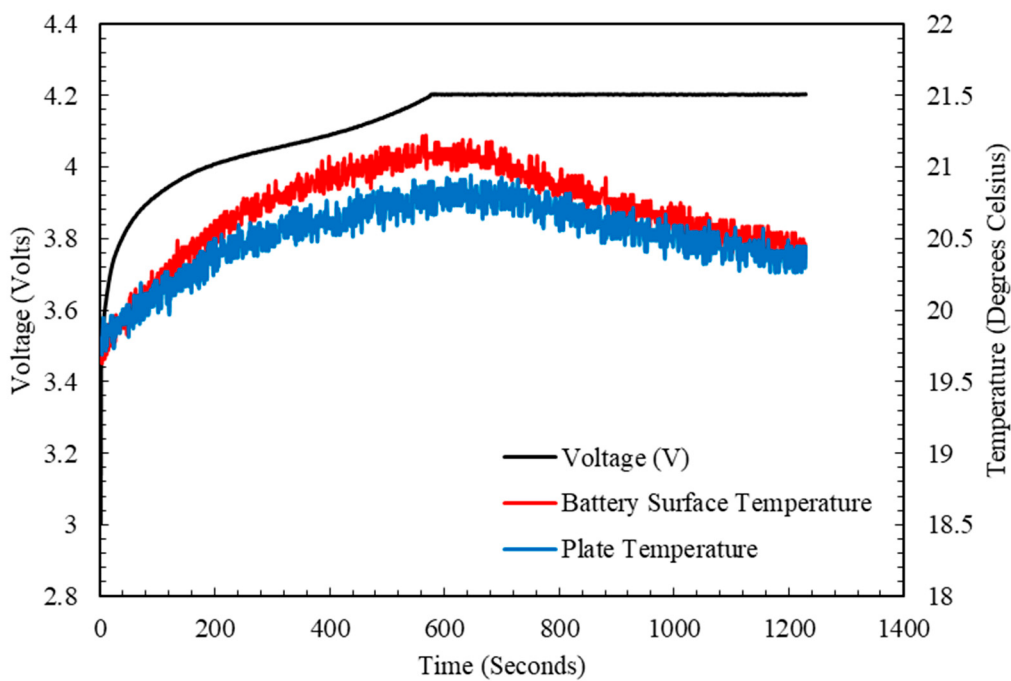


Figure 9. Battery-surface and plate-surface temperatures during fast charging.

4.3. LPM Parameters

Some parameters of the LPM were obtained from the literature while others were identified by fitting the model to the experimental data. The thermal conductivity of the cell for the LPM, for example, can be determined by combining the material properties reported in the literature. The thermal conductivity of a battery cell, composed of many layers of different conductivities, will vary depending on the direction of heat flow [30,37]. The through-plane thermal conductivity, in the direction of the heat flow considered in the LPM, can be expressed as [37]:

$$\frac{\sum t_v}{K_{eq}} = \sum \frac{t_v}{K_v} \quad (26)$$

where K_v is the thermal conductivity of the material layer and t_v is the thickness of the material layer. The equivalent thermal conductivity of the cell, thus determined, is found to be $0.633 \frac{W}{mK}$. The thermal conductivity and thermal expansion coefficient of the plate are $167 \frac{W}{mK}$, and $25.2 \times 10^{-6} \frac{1}{K}$, respectively, from the literature.

The experimental data used for tuning of the remaining LPM parameters include those collected during CC discharging from 3.6 to 3 volts, CC fast charging from 3 to 4.2 volts, and CC discharging from 4.2 to 3 volts. The responses and predictors of the LPM are summarized in Table 3. Four LPM parameters were estimated based on the experimental data: (1) the heat capacity of the cell, C_{Cell} , (2) the heat transfer coefficient of air, h_{air} , (3) the thermal expansion coefficient of the cell, α_{Cell} , and (4) the SOC coefficient for expansion due to lithiation, ξ . The parameters were estimated such that the sum of squared errors in predicting the temperatures, $T_{s,1}$ and $T_{s,2}$, the force, F , and the displacement, $\delta^{EXP,\%}$, is minimized as follows:

$$\min \sum_i \left(T_{s,1}^{actual} - T_{s,1}^{predicted} \right)^2 + \left(T_{s,2}^{actual} - T_{s,2}^{predicted} \right)^2 + \left(F^{actual} - F^{predicted} \right)^2 + \left(\delta_{Total}^{EXP,\%,actual} - \delta_{Total}^{EXP,\%,predicted} \right)^2 \quad (27)$$

Table 3. Responses and predictors of the LPM.

Responses	Symbol
Battery surface temperature	$T_{s,1}$
Plate surface temperature	$T_{s,2}$
Total force	F
Displacement of the fixture	$\delta^{EXP,\%}$
Predictors	Symbol
Heat generated from the battery	Q_{gen}
Diffusion swelling	$\delta_{Diffusion}^{\%}$
Time	Time
Ambient temperature	T_{Amb}

A non-linear regression was performed using the least-squares curve fitting in MATLAB. The parameter values, thus estimated, are listed in Table 4. The estimated parameter values are in the same order of magnitude as those in the literature, e.g., in [15]. The results of model-fitting are shown in Figure 10. The experimental battery surface temperature, the plate surface temperature, and the fixture displacement are in good agreement with the LPM predictions. However, a relatively large error in prediction of force can be observed at the end of charging and during discharging.

Table 4. Estimated LPM parameters.

Parameters	Optimization Solution
$C_{Cell} \cdot (\text{J/K})$	451.62
$h_{air} \cdot (\text{W/m}^2\text{K})$	95.743
$\alpha_{Cell} \cdot (\text{1/K})$	4.39×10^{-4}
$\xi \cdot (\text{m})$	1.03×10^{-4}

In order to evaluate the goodness of model-fitting, the root mean square error (RMSE) is calculated (see Table 5):

$$\text{RMSE} = \sqrt{\frac{\sum_{i=1}^N (y_i^{actual} - y_i^{predicted})^2}{N}} \quad (28)$$

where y_i^{actual} is the experimental value, $y_i^{predicted}$ is the value predicted in the model, and N is the number of data points. Additionally, the RMSE divided by the range and average are also listed. It can be seen that, for each output, its RMSE is below 20% of its range indicating a good model-fit.

Table 5. Maximum error and RMSE between the experimental and predicted curves.

Responses	Maximum Error	RMSE	RMSE/ Range	RMSE/ Average
$T_{s,1}$	0.52	0.1326	0.1262	0.0066
$T_{s,2}$	0.63	0.1190	0.1142	0.0060
$\delta^{EXP,\%}$	6.06×10^{-6}	3.6364×10^{-6}	0.0968	0.2960
F	573	297.73	0.1922	0.1800

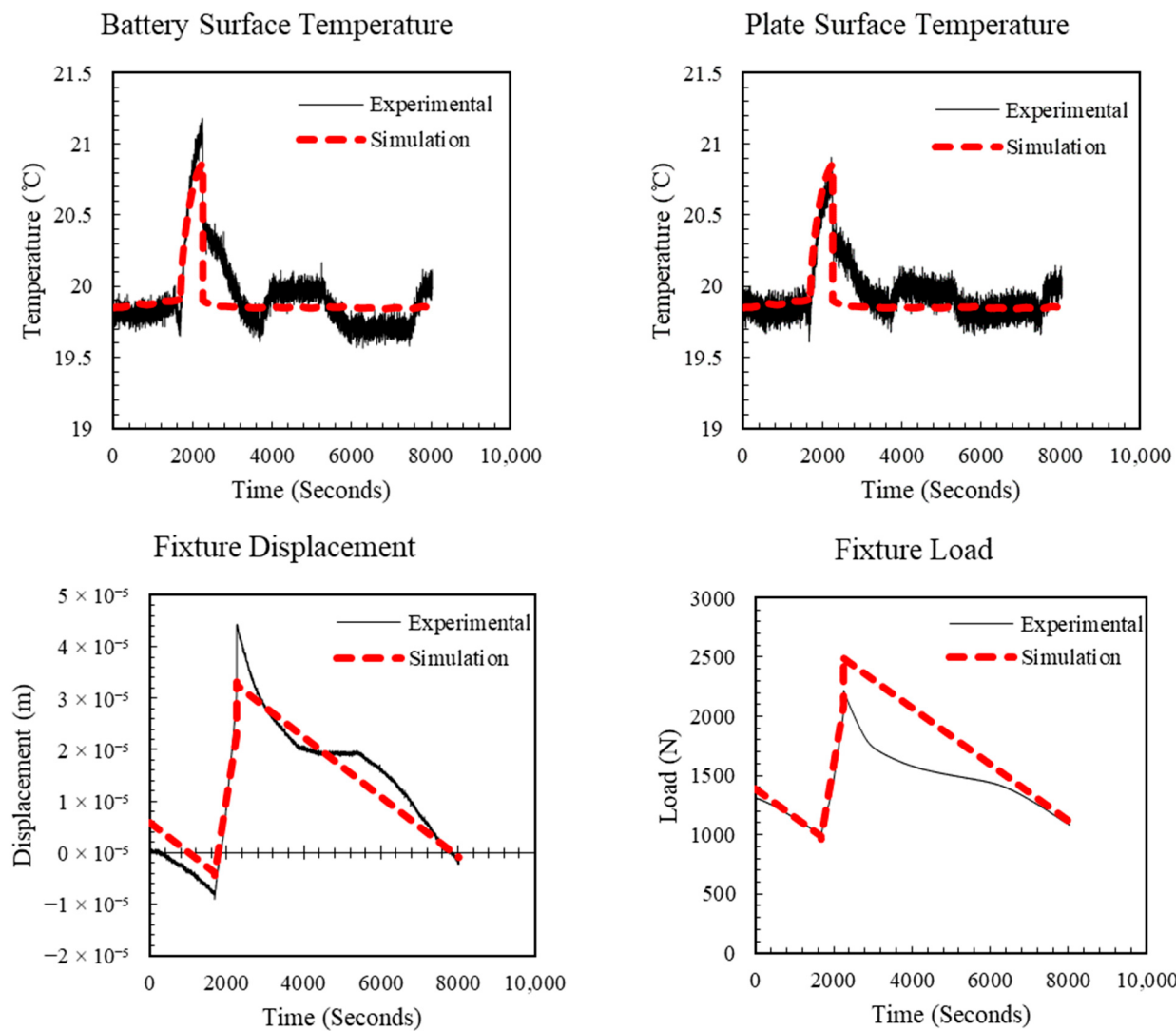


Figure 10. Comparison of the simulated output and the experimental data after model fitting.

5. Simulation Study

As mentioned in the introduction, a significant degradation in the separator's integrity can be observed after the battery cell undergoes cyclic 4C charging [8]. Therefore, the stress in the separator under 4C charging is estimated using the developed hybrid model. Moreover, the effect of charging rate, pre-torque, and ambient temperature on the stress in the separator is investigated.

5.1. Estimated Stress in the Separator

The stress in the separator under 4C charging condition of the cycling test in [8] was calculated using the hybrid model. Specifically, the core temperature, boundary pressure, and lithium concentration predicted using the electrochemical model and the LPM model were used as inputs for the solid mechanics model (See Figure 1). Figure 11a shows a homogeneous distribution of the von Mises stress in the middle section of the separator at the end of 4C charging, while Figure 11b presents the evolution of the maximum von Mises stress over time during charging. The von Mises stress is calculated as follows [38]:

$$\sigma_{\text{Mises}} = \frac{\sqrt{2}}{2} \left[(\sigma_1 - \sigma_2)^2 + (\sigma_2 - \sigma_3)^2 + (\sigma_3 - \sigma_1)^2 \right]^{\frac{1}{2}} \quad (29)$$

where σ_1 , σ_2 , and σ_3 are the principal stress components. The von Mises stress serves as a measure of the overall stress experienced by the material at a specific location, accounting for both normal and shear stresses.

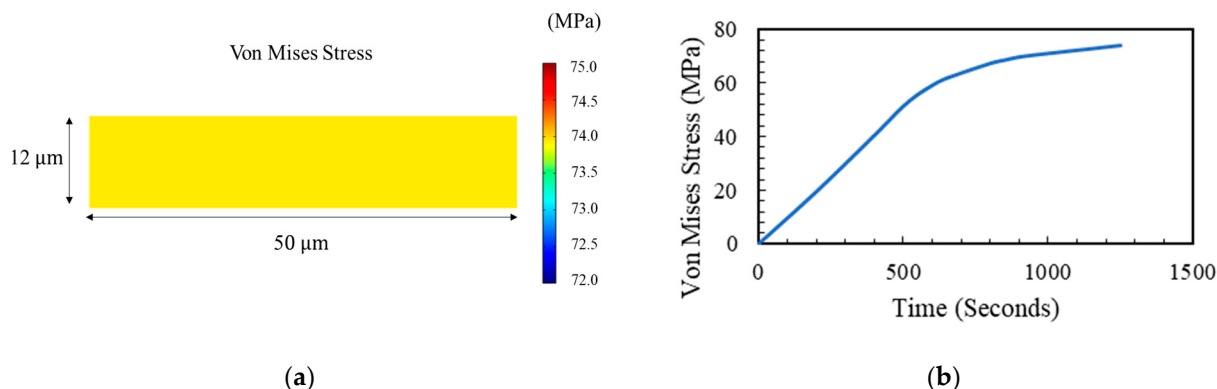


Figure 11. Von Mises stress in the separator. (a) Stress distribution at the end of charging. (b) Evolution of stress during charging.

The von Mises stress showed a homogeneous distribution within the central part of the separator during the 4C charging. The maximum von Mises stress is found to be 74.1 MPa at the end of fast charging. Creep and fatigue behavior of the separator under the estimated stress will be presented in Section 6.

5.2. Effect of Charging Rate

The hybrid model allows examination of the effect of charging rate on the separator. Evolution of the von Mises stress in the separator over time was analyzed at four different charging rates of 1C, 2C, 4C, and 5C with other conditions, such as the pre-torque and ambient temperature, fixed at those in Section 5.1. The CC–CV charging protocol was employed for each charging rate. Figure 12 shows the temperature variations during charging for different charging rates. When the charging rate is 1C, the cell temperature slightly increases from 20 °C to the maximum value of 20.25 °C at the end of the constant current (CC) period. As the charging rate increases, the maximum cell temperature increases, e.g., 24.6 °C at 5C. It can be seen that a higher charging rate results in an elevated cell temperature, which can potentially compromise battery safety and lead to accelerated degradation of cell components including the separator. Therefore, a careful consideration of the charging rate is essential for optimal battery performance and longevity.

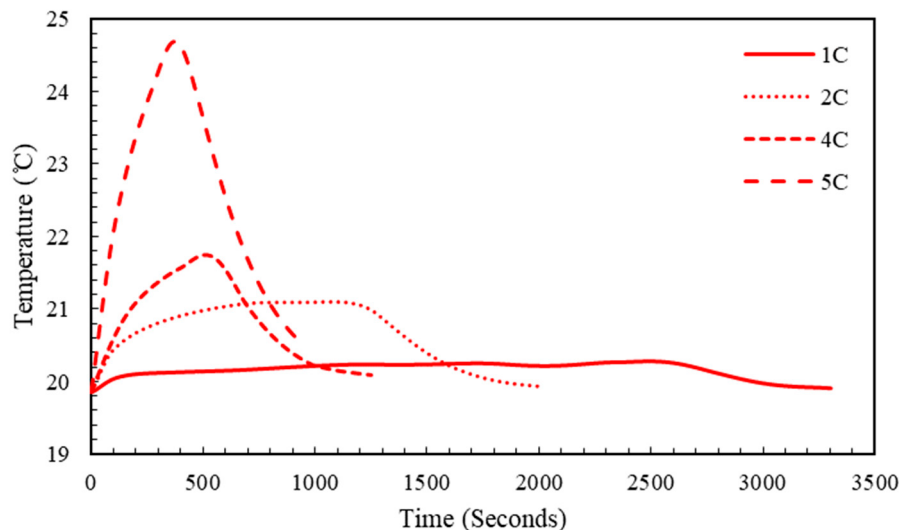


Figure 12. Evolution of cell temperature during 1C, 2C, 4C, and 5C charging.

Evolution of the von Mises stress in the separator over time at the four different charging rates is shown in Figure 13. Regardless of the charging rate, the von Mises stress exhibits a linear increase during the constant charge (CC) period followed by a slower increase during the constant voltage (CV) period. A faster increase in the von Mises stress is observed with an increase in the charging rate. It should be noted that the proposed hybrid model is capable of predicting the evolution of stress for any charging protocols. The hybrid model, therefore, opens the possibility of optimizing the charging schedule for achieving multiple objectives such as prolonging both electrode health and separator integrity.

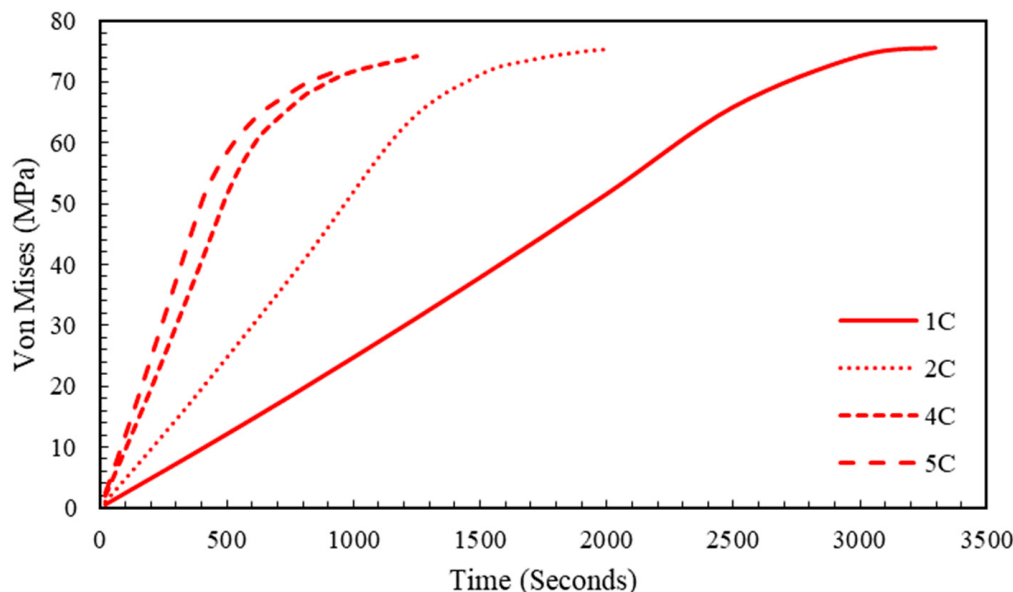


Figure 13. Von Mises stress evolution in the middle of the separator.

5.3. Effect of Pre-Torque

The effect of pre-torque on separator stress is examined by applying various pre-torque values to the hybrid model. Different pre-torques ranging from 0.5 to 12 N·m were simulated. Note, in the experiment in Section 3, a pre-torque of 1 N·m was applied to the fixture. Figure 14 shows only a minor change in the von Mises stress with increasing pre-torque. The reason why the pre-torque plays a minor role in the separator stress is as follows. The stress in the separator can be attributed to two main mechanisms. First, during charging, the anode expands in all directions due to lithiation and a temperature increase. Expansion of anode will exert a tensile load on the separator as the anode pulls the separator in the horizontal direction, as seen in Figure 5. Second, the pressure due to the pre-torque and structural constraint imposed by the fixture will compress the separator in the vertical direction. The stress due to pulling is much larger than the one due to the pressure by at least two orders in this particular configuration. Therefore, the change in pressure due to varying pre-torque will have only a minor effect on the von Mises (overall) stress.

5.4. Effect of Ambient Temperature

The effect of ambient temperature on separator stress was investigated by applying six different ambient temperatures ranging from 0 to 50 °C to the hybrid model. Figure 15 shows the relationship between the von Mises stress in the separator at the end of charging and the ambient temperature. The results show a decrease in the von Mises stress with increasing ambient temperature.

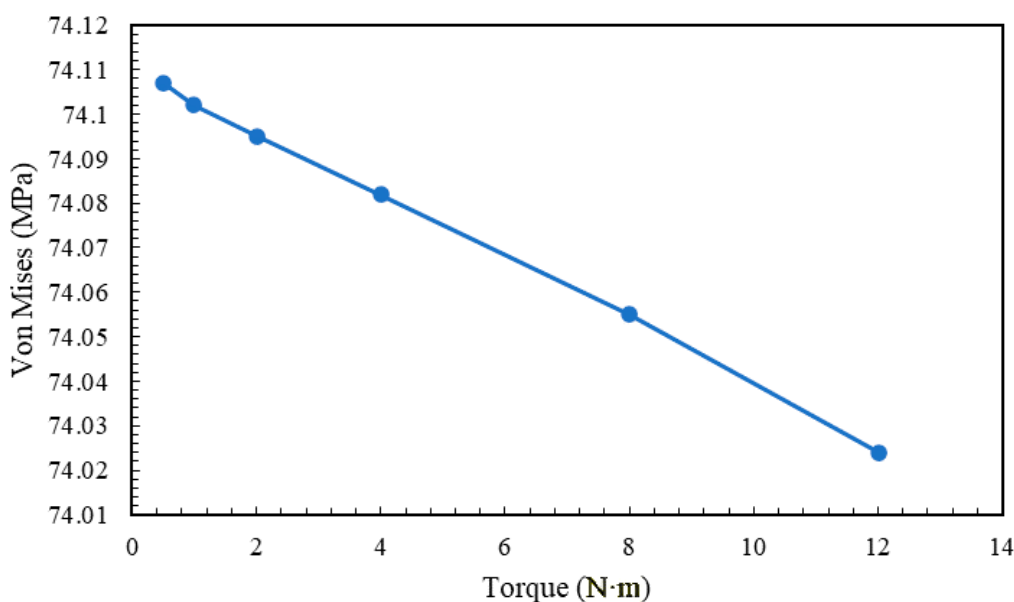


Figure 14. Von Mises stress at different torques.

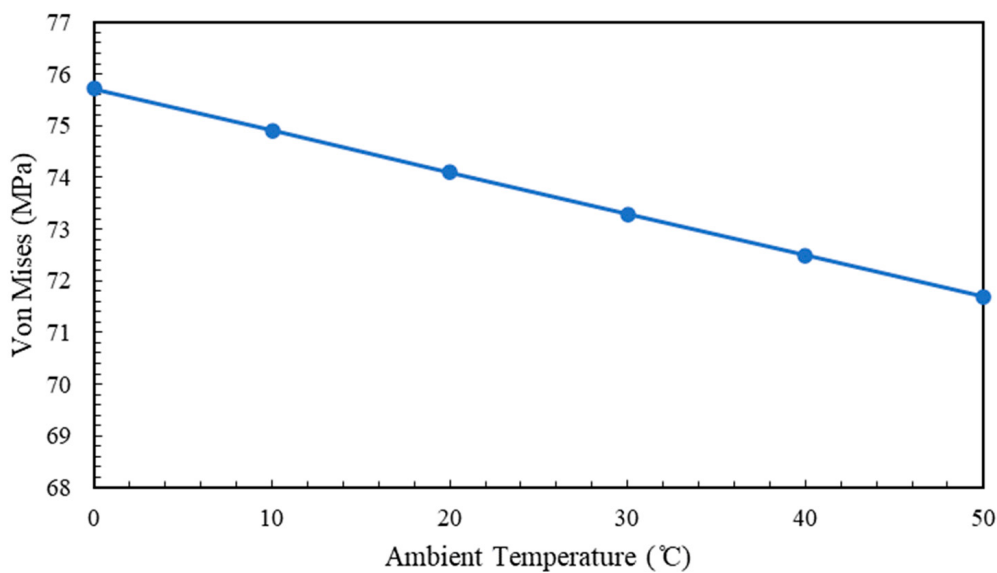


Figure 15. Von Mises stress at different ambient temperatures.

The cell temperature will increase when the ambient temperature rises. This will lead to expansion of battery components in both horizontal and vertical directions (see Figure 5). Since the thermal expansion coefficient of the separator is significantly larger than those of the other battery components, the separator will experience a pronounced length expansion in the horizontal direction, which leads to less pulling by the anode and lower stresses.

6. Creep and Fatigue Testing

As previously discussed, noticeable degradation of the separators' mechanical properties (by as much as 50%) was observed when the LIB, made of the same separator as the one in this study, was subject to repeated fast (4C) charging [8]. In Section 5, the maximum von Mises stress during 4C charging was found to be 74 MPa while only a small temperature rise was observed. Therefore, creep and fatigue tests were carried out on a pristine separator at room temperature to examine its behavior under the estimated stress during 4C charging.

Strip-shaped uniaxial tensile specimens were prepared according to ASTM D882. The samples were cut from a new separator roll using a razor. The longer axis the sample was aligned in the machine direction was with a length of 100 mm and a width of 10 mm. The gage length was chosen to be 50 mm. The creep and fatigue experiments were conducted using an ElectroPuls E1000. Foamy jaws were used to hold the specimen from each end.

Creep testing was conducted at five target stresses ranging from 50 to 90 MPa, which are lower than the yield stress of the separator (ranging from 100 to 140 MPa in the machine direction depending on the strain rate, according to the authors' previous study [8]). Note the maximum von Mises stress during 4C charging was estimated at 74.1 MPa in Section 5.1. In each creep testing, the loading increased linearly from 0 MPa to the target stress at a rate of 0.1 MPa/s. Once a target stress is reached, the loading remained at the same stress level until the displacement reaches 60 mm (except for the target stress of 50 MPa since the maximum duration of the creep test was 6 days). The creep test results are presented in Figure 16. The samples subjected to 90 and 80 MPa reached 60 mm displacement in 4 and 5.5 h, respectively. Both tests remained in the primary stage of creep, characterized by a rapid deformation. The time required to reach 60 mm displacement increases significantly to 37 h under the stress of 70 MPa, while that under the stress of 60 MPa reaches in 68 h. At 50 MPa, the test stopped after 6 days when its displacement reached 48.45 mm. The results of creep tests at 50, 60, and 70 MPa exhibit the secondary creep stage where the creep becomes more gradual after the primary creep stage. The creep test results indicate that the stress during 4C charging can cause permanent damage to the separator. The results suggest that tensile creep is a major factor contributing to the mechanical degradation of the battery separator.

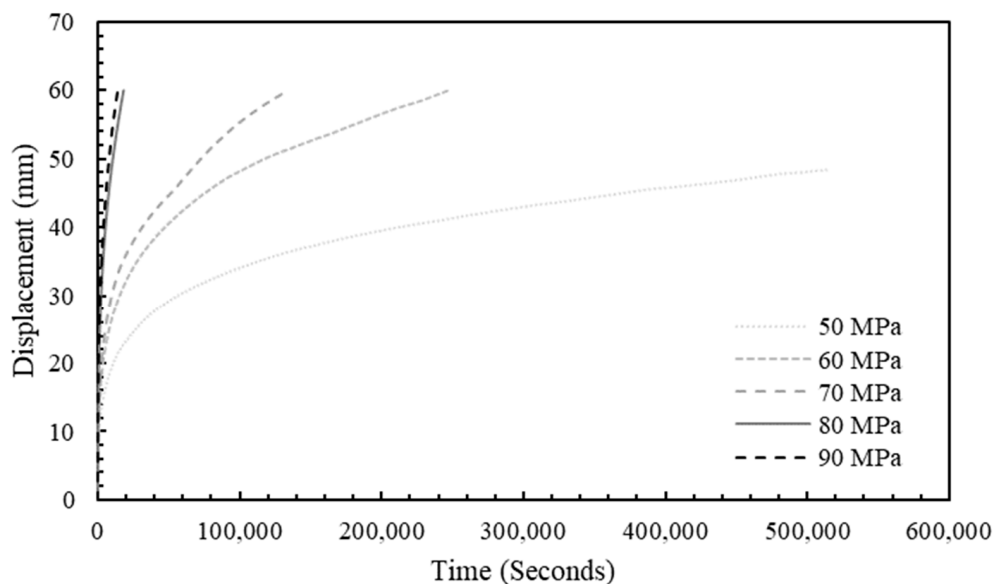


Figure 16. Displacement over time in creep tests.

The fatigue test was designed to mimic the stress evolution in the separator during cyclic fast charging for 68 cycles. Each cycle consists of (1) an increasing load along a linear ramp (0 to 70 MPa in 13 min) representing a 4C charging duration, (2) a stress hold representing a CV period for 10 min, and (3) a linear decreasing ramp (70 to 0 MPa in 90 min) representing a discharging duration. Figure 17 shows the variations of load and displacement over time during the first cycle. The displacement curve shows a rapid increase during the charging period, followed by a gradual increase in the displacement during the holding period and the beginning part of discharging. This is followed by decrease in the displacement for the remaining period of discharging. Even after the load returns to 0, a non-zero elongation of 1.3 mm remains, indicating a permanent damage in the separator.

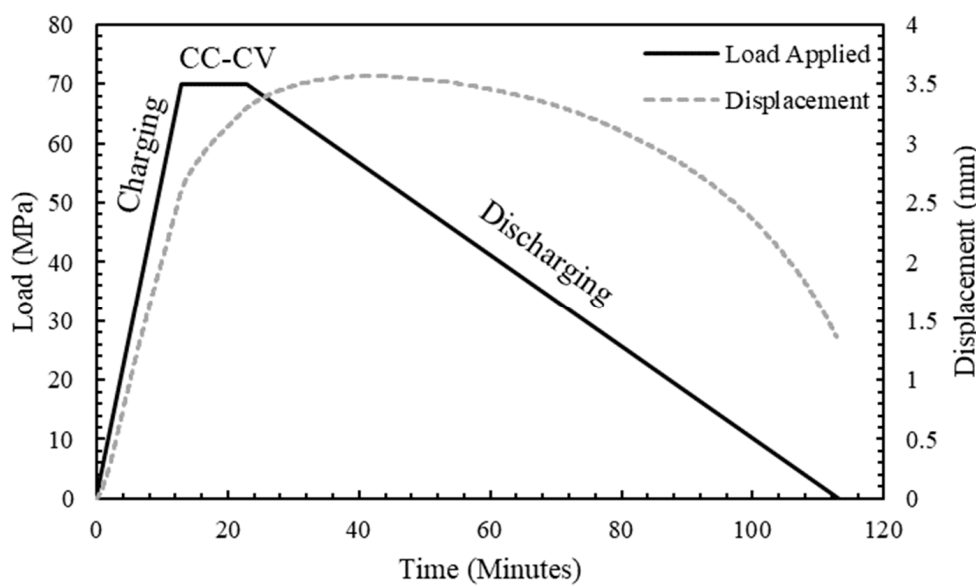


Figure 17. Load and displacement versus time.

The results of fatigue testing for 68 cycles are shown in Figure 18. The displacement over time is shown in Figure 18a while the maximum displacement of each cycle is plotted in Figure 18b. In Figure 18b, the displacement increases rapidly during the first 10 cycles and then shows a linear increase for the remaining cycles. It should be noted that the fatigue test demonstrates an extreme case of separator degradation during cycling. Once the separator elongates permanently after the first few cycles, it will be subject to stresses much lower than 70 MPa in the proceeding cycles. Nevertheless, the test results indicate that the load on the separator during 4C charging is high enough to cause damage to the separator. Moreover, the damage can be accumulated in the separator via repeated loading, explaining the separator degradation after cyclic fast charging in the previous study [8].

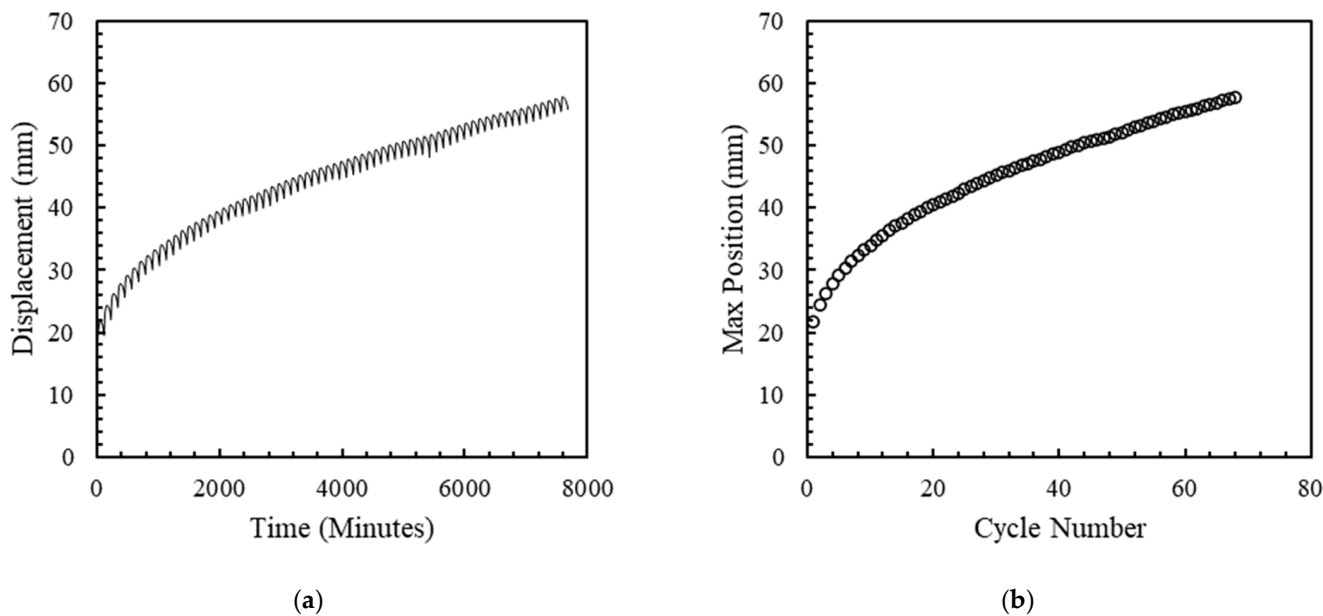


Figure 18. Results of fatigue testing. (a) Displacement over time. (b) Maximum position of each cycle.

7. Conclusions

Combining three sub-models enabled predicting the stress in the separator under various use conditions including those for battery pack assembly and thermal management.

The parameters of a lumped-parameter model were determined based on the experimental data showing good model-fit, while the material properties in other sub-models were obtained from the literature. The developed model allowed estimating the maximum von Mises stress as 74 MPa during the fast-charging condition, under which a significant separator degradation was observed after 1600 cycles in the previous study. In order to investigate the damage to the separator under this loading condition, creep and fatigue tests were conducted on a pristine separator. The high creep sensitivity and creep deformation in the test results indicate that such loading can produce and accumulate significant damage in the separator. However, care should be taken to avoid concluding that the mechanical stress is the only driving force behind separator degradation. The high temperature, which was not considered due to the low temperature rise of the setup in this study, may play a role by causing thermal degradation, which is a major mechanism for degradation of polymers in general. While the current state of the model allows for an efficient way in predicting the stresses in the cell across various charge rates, torque levels, and ambient temperature conditions, further investigations should be conducted to explore a more complex solid mechanics model which includes plasticity and damage in the constitutive equations. Additionally, the model can be further improved by incorporating concentration-dependent material properties to improve the mechanical predictions.

Author Contributions: Conceptualization, M.M., C.W.L. and G.A.; methodology, M.M., C.W.L. and G.A.; software, M.M.; validation, M.M., C.W.L. and G.A.; formal analysis, M.M.; investigation, M.M.; resources, M.M., C.W.L. and G.A.; data curation, M.M.; writing—original draft preparation, M.M.; writing—review and editing, M.M. and C.W.L.; visualization, M.M.; supervision, M.M., C.W.L. and G.A.; project administration, C.W.L.; funding acquisition, C.W.L. and G.A. All authors have read and agreed to the published version of the manuscript.

Funding: The research was partly funded by Ford Motor Company (Ford-UM Alliance: Development of a Lithium Ion Battery Separator Aging Model).

Data Availability Statement: Data will be available on request.

Acknowledgments: The authors would like to thank Tom Brackett for conducting the Li-ion batteries charging and discharging test.

Conflicts of Interest: The authors declare no conflict of interest.

Nomenclature

A	Area
a	Particle specific surface area
C_{cell}	Cell heat capacity
c	Lithium concentration
D	Diffusion coefficient
E	Young's modulus
F	Force
F_r	Faraday's constant
h_{air}	Convection heat transfer coefficient of air
I_{app}	Current density
i_{ex}	Exchange current density
J	Pore wall flux
k_i	Reaction rate constant
K	Thermal conductivity
L	Thickness
Q_{conv}	Convective heat transfer
Q_{gen}	Heat generation rate
R	Ideal gas constant

r	Particle radius coordinate
r_p	Particle radius
s	Spring constant
T	Temperature
t	Time
t_+	Transport number
U	Open circuit potential
V	Volume
α	Thermal expansion coefficient
α_a	Charge transfer coefficient for oxidation
α_c	Charge transfer coefficient for reduction
δ	Displacement
δ_{ij}	Kronecker delta
ε	Volume fraction
ϵ	Mechanical strain
η	Overpotential of the intercalation reaction
κ	Electrolyte ionic conductivity
ν	Poisson's ratio
ξ	Coefficient of expansion for state-of-charge
σ	Mechanical stress
τ_{eff}	Effective conductivity
ϕ	Potential
Δ	Displacement due to bolt
ΔL	Swelling
Ω	Partial molar volume
Superscripts	
i	Electrode under consideration (p for positive electrode and n for negative electrode)
n	Negative electrode
p	Positive electrode
sep	Separator
v	Component under consideration (p for cathode, n for anode, and sep for separator)
Subscripts	
eff	Effective
$filler$	Binder and fillers
l	Liquid phase
s	Solid phase
$surf$	On the surface

References

1. Bandhauer, T.M.; Soc, J.E.; Bandhauer, T.M.; Garimella, S.; Fuller, T.F. A Critical Review of Thermal Issues in Lithium-Ion Batteries. *J. Electrochem. Soc.* **2011**, *158*, R1. [[CrossRef](#)]
2. Lukic, S.M.; Cao, J.; Bansal, R.C.; Rodriguez, F.; Emadi, A. Energy Storage Systems for Automotive Applications. *IEEE Trans. Ind. Electron.* **2008**, *55*, 2258–2267. [[CrossRef](#)]
3. Arora, P.; Zhang, Z. Battery Separators. *Chem. Rev.* **2004**, *104*, 4419–4462. [[CrossRef](#)]
4. Lee, H.; Yanilmaz, M.; Toprakci, O.; Fu, K.; Zhang, X. A Review of Recent Developments in Membrane Separators for Rechargeable Lithium-Ion Batteries. *Energy Environ. Sci.* **2014**, *7*, 3857–3886. [[CrossRef](#)]
5. Baldwin, R.S.; Bennet, W.R.; Wong, E.K.; Lewton, M.R.; Harris, M.K. *Battery Separator Characterization and Evaluation Procedures for NASA's Advanced Lithium-Ion Batteries*; National Aeronautics and Space Administration: Cleveland, OH, USA, 2010.
6. Zhou, W. Effects of External Mechanical Loading on Stress Generation during Lithiation in Li-Ion Battery Electrodes. *Electrochim. Acta* **2015**, *185*, 28–33. [[CrossRef](#)]
7. Huang, X. Separator Technologies for Lithium-Ion Batteries. *J. Solid State Electrochem.* **2011**, *15*, 649–662. [[CrossRef](#)]
8. Makki, M.; Ayoub, G.; Lee, C.W.; Bae, C.; Colin, X. Effect of Battery Fast Cyclic Charging on the Mechanical and Fracture Behavior of the Lithium-Ion Battery Separator. *Polym. Degrad. Stab.* **2023**, *216*, 110469. [[CrossRef](#)]
9. Liu, B.; Jia, Y.; Yuan, C.; Wang, L.; Gao, X.; Yin, S.; Xu, J. Safety Issues and Mechanisms of Lithium-Ion Battery Cell upon Mechanical Abusive Loading: A Review. *Energy Storage Mater.* **2020**, *24*, 85–112. [[CrossRef](#)]
10. Christensen, J.; Newman, J. Stress Generation and Fracture in Lithium Insertion Materials. *J. Solid State Electrochem.* **2006**, *10*, 293–319. [[CrossRef](#)]

11. Gor, G.Y.; Cannarella, J.; Prévost, J.H.; Arnold, C.B. A Model for the Behavior of Battery Separators in Compression at Different Strain/Charge Rates. *J. Electrochem. Soc.* **2014**, *161*, F3065–F3071. [[CrossRef](#)]
12. Peabody, C.; Arnold, C.B. The Role of Mechanically Induced Separator Creep in Lithium-Ion Battery Capacity Fade. *J. Power Sources* **2011**, *196*, 8147–8153. [[CrossRef](#)]
13. Xiao, X.; Wu, W.; Huang, X. A Multi-Scale Approach for the Stress Analysis of Polymeric Separators in a Lithium-Ion Battery. *J. Power Sources* **2010**, *195*, 7649–7660. [[CrossRef](#)]
14. Shi, D.; Xiao, X.; Huang, X.; Kia, H. Modeling Stresses in the Separator of a Pouch Lithium-Ion Cell. *J. Power Sources* **2011**, *196*, 8129–8139. [[CrossRef](#)]
15. Oh, K.Y.; Epureanu, B.I. A Novel Thermal Swelling Model for a Rechargeable Lithium-Ion Battery Cell. *J. Power Sources* **2016**, *303*, 86–96. [[CrossRef](#)]
16. Oh, K.Y.; Epureanu, B.I.; Siegel, J.B.; Stefanopoulou, A.G. Phenomenological Force and Swelling Models for Rechargeable Lithium-Ion Battery Cells. *J. Power Sources* **2016**, *310*, 118–129. [[CrossRef](#)]
17. Xu, J.; Wang, L.; Guan, J.; Yin, S. Coupled Effect of Strain Rate and Solvent on Dynamic Mechanical Behaviors of Separators in Lithium Ion Batteries. *Mater. Des.* **2016**, *95*, 319–328. [[CrossRef](#)]
18. Xu, J.; Liu, B.; Wang, X.; Hu, D. Computational Model of 18650 Lithium-Ion Battery with Coupled Strain Rate and SOC Dependencies. *Appl. Energy* **2016**, *172*, 180–189. [[CrossRef](#)]
19. Liu, B.; Zhao, H.; Yu, H.; Li, J.; Xu, J. Multiphysics Computational Framework for Cylindrical Lithium-Ion Batteries under Mechanical Abusive Loading. *Electrochim. Acta* **2017**, *256*, 172–184. [[CrossRef](#)]
20. Duan, X.; Wang, H.; Jia, Y.; Wang, L.; Liu, B.; Xu, J. A Multiphysics Understanding of Internal Short Circuit Mechanisms in Lithium-Ion Batteries upon Mechanical Stress Abuse. *Energy Storage Mater.* **2022**, *45*, 667–679. [[CrossRef](#)]
21. Yuan, C.; Wang, L.; Yin, S.; Xu, J. Generalized Separator Failure Criteria for Internal Short Circuit of Lithium-Ion Battery. *J. Power Sources* **2020**, *467*, 228360. [[CrossRef](#)]
22. Doyle, M.; Fuller, T.F.; Newman, J. Modeling of Galvanostatic Charge and Discharge of the Lithium / Polymer / Insertion Cell. *J. Electrochem. Soc.* **1993**, *140*, 1526–1533. [[CrossRef](#)]
23. Doyle, M.; Newman, J. Comparison of Modeling Predictions with Experimental Data from Plastic Lithium Ion Cells Comparison of Modeling Predictions with Experimental Data from Plastic Lithium Ion Cells. *J. Electrochem. Soc.* **1996**, *143*, 1890. [[CrossRef](#)]
24. Smith, K.A.; Rahn, C.D.; Wang, C. Model Order Reduction of 1D. *J. Dyn. Syst. Meas. Control* **2008**, *130*, 1–8. [[CrossRef](#)]
25. Smith, K.A.; Rahn, C.D.; Wang, C. Control Oriented 1D Electrochemical Model of Lithium Ion Battery. *Energy Convers. Manag.* **2007**, *48*, 2565–2578. [[CrossRef](#)]
26. Lin, X.; Perez, H.E.; Siegel, J.B.; Stefanopoulou, A.G.; Li, Y.; Anderson, R.D.; Ding, Y.; Castanier, M.P. On-Line Parameterization of Lumped Thermal Dynamics in Cylindrical Lithium Ion Batteries for Core Temperature Estimation and Health Monitoring. *IEEE Trans. Control Syst. Technol.* **2012**, *21*, 1745–1755.
27. Lin, X.; Perez, H.E.; Mohan, S.; Siegel, J.B.; Stefanopoulou, A.G.; Ding, Y.; Castanier, M.P. A Lumped-Parameter Electro-Thermal Model for Cylindrical Batteries. *J. Power Sources* **2014**, *257*, 1–11. [[CrossRef](#)]
28. Kim, Y.; Siegel, J.B.; Stefanopoulou, A.G. A Computationally Efficient Thermal Model of Cylindrical Battery Cells for the Estimation of Radially Distributed Temperatures. In Proceedings of the 2013 American Control Conference, Washington, DC, USA, 17–19 June 2013; IEEE: Piscataway, NJ, USA; pp. 698–703.
29. Bernardi, D.; Pawlikowski, E.; Newman, J. A General Energy Balance for Battery Systems. *J. Electrochem. Soc.* **1985**, *132*, 5. [[CrossRef](#)]
30. Chen, S.C.; Wan, C.C.; Wang, Y.Y. Thermal Analysis of Lithium-Ion Batteries. *J. Power Sources* **2005**, *140*, 111–124. [[CrossRef](#)]
31. Zhang, X.; Shyy, W.; Marie Sastry, A. Numerical Simulation of Intercalation-Induced Stress in Li-Ion Battery Electrode Particles. *J. Electrochem. Soc.* **2007**, *154*, A910. [[CrossRef](#)]
32. Zhang, X.; Sastry, A.M.; Shyy, W. Intercalation-Induced Stress and Heat Generation within Single Lithium-Ion Battery Cathode Particles. *J. Electrochem. Soc.* **2008**, *155*, A542. [[CrossRef](#)]
33. Bulla, M.; Kolling, S.; Sahraei, E. A Material Model for the Orthotropic and Viscous Behavior of Separators in Lithium-Ion Batteries under High Mechanical Loads. *Energies* **2021**, *14*, 4585. [[CrossRef](#)]
34. Bulla, M.; Kolling, S.; Sahraei, E. An Experimental and Computational Study on the Orthotropic Failure of Separators for Lithium-Ion Batteries. *Energies* **2020**, *13*, 4399. [[CrossRef](#)]
35. Makki, M.; Ayoub, G.; Lee, C.W. Modeling the Anisotropic Behavior of Highly Orthotropic Lithium-Ion Batteries Polymer Separators. *Int. J. Solids Struct.* **2023**, *264*, 112102. [[CrossRef](#)]
36. Zhou, W.; Hao, F.; Fang, D. The Effects of Elastic Stiffening on the Evolution of the Stress Field within a Spherical Electrode Particle of Lithium-Ion Batteries. *Int. J. Appl. Mech.* **2013**, *5*, 1350040. [[CrossRef](#)]
37. Drake, S.J.; Wetz, D.A.; Ostanek, J.K.; Miller, S.P.; Heinzel, J.M.; Jain, A. Measurement of Anisotropic Thermophysical Properties of Cylindrical Li-Ion Cells. *J. Power Sources* **2014**, *252*, 298–304. [[CrossRef](#)]
38. Dieter, D.E. *Mechanical Metallurgy*, 3rd ed.; McGraw-Hill Publishing Company: New York, NY, USA, 1986.